

Hydrodynamic Effects in Cryogenic Buffer Gas Cells: Design Insights from Hybrid Simulations

Nick Vogeley¹, Bernd Bauerhenne², Daqing Wang¹‡

¹Institute of Applied Physics, University of Bonn, Wegelerstr. 8, 53115 Bonn, Germany

²Experimentalphysik I, University of Kassel, Heinrich-Plett-Str. 40, 34132, Kassel, Germany

Abstract. Cryogenic buffer gas beam sources have become an essential tool for experiments requiring cold molecular beams with low forward velocities. Although recent experimental advances have led to significant progress in source optimization, numerical studies remain limited due to the challenges posed by the large parameter ranges required to describe both the dense buffer gas and the dilute seed molecules. In this work, we report a numerical evaluation of cryogenic buffer gas beam cells operating in the hydrodynamic extraction regime. While most prior studies focused on box-like or cylindrical cells, we investigated hydrodynamic effects including vortex formation in a spherical cell and assessed whether these could be utilized to enhance the performance in molecule cooling and extraction. To achieve this, we performed steady-state slip-flow simulations for helium buffer gas and employed a direct-simulation Monte Carlo diffusion routine to track particle trajectories. We compared the performance of the source across different buffer gas throughputs and injection angles and identified parameter regimes where vortex formation enhances molecule extraction. From the simulations, we extracted experimental observables, which allow these effects to be verified through velocity or time-of-flight measurements on the molecular beam.

1. Introduction

Production of cold molecules is essential for a broad spectrum of experimental investigations across multiple disciplines. In particular, cold beams could enable the study of quantum-state-resolved chemical reactions [1, 2], provide laboratory analogues for astrochemical environments [3], and serve as platforms for quantum information [4] and precision spectroscopy [5–7]. Among various techniques for cold molecular beam generation, cryogenic buffer gas beam (CBGB) sources [8, 9] have become a workhorse for experiments that require both low forward velocity and low internal temperatures. CBGB source utilizes pre-cooled inert buffer gas, typically helium or neon, to mix with seed molecules in a cryogenic cell. Through collisions, the molecules thermalize with the buffer gas and are subsequently entrained through an orifice, forming a cold molecular beam. An advantage of CBGB over traditional seeded supersonic sources is the forward speed of the beam, which can be lowered

‡ Email: daqing.wang@uni-bonn.de

to the order of $100 \text{ m} \cdot \text{s}^{-1}$, which is particularly advantageous for experiments that require slow beams. The combination of low forward velocities and low internal temperatures has enabled a series of recent experimental advances, including laser cooling and trapping of polyatomic molecules [10,11], spectroscopy of atomic species that lack cycling transitions [12,13] and organic fluorophores [14,15].

However, the trade-off is the higher complexity of the experimental setup along with the overhead in maintaining and optimizing the source performance. Despite numerous experimental advances in improving CBGB sources, e.g., in terms of reducing forward velocity [16] and improving phase space density [17], there has been only a limited number of numerical investigations [18–21]. The challenge in simulating buffer gas cells lies in the large mismatch in the parameter regime of the buffer gas and seed molecules in terms of density, pressure and temperature, which precludes the usage of a single solver and necessitates a hybrid approach that combines different simulation methods [20]. Therefore, a large parameter space of the CBGB design, including cell geometry, buffer gas injection angle, throughput, and orifice design, remains to be explored. Further systematic computational studies are therefore essential to enable the predictive design of CBGB sources and to support their broader applications across a wider range of molecular species.

In this article, we present a hybrid numerical investigation [22] that combines flow dynamics and single-particle tracing to understand and optimize a spherical-shaped CBGB cell. In the flow range of $J \approx 20 \text{ sccm}$, we identify the emergence of a hydrodynamical effect that enhances molecular extraction and suppresses contamination of the inner walls of the buffer gas cell. These findings provide a foundation for future experimental validation, e.g., through measurements on the beam velocity and density. We anticipate that this study will contribute to the advancement of numerically guided design strategies for cold molecular beam sources.

2. Cell Geometry

The configuration of the buffer gas cell considered in this work is illustrated in Fig. 1. This geometry is conceptualized for easy machinability from a solid copper block using a minimal set of bores. The main body of the cell consists of a cylindrical volume with a diameter of $D = 16 \text{ mm}$ and a height of 8 mm . The upper end of the cylinder is enclosed by a hemispherical cap of the same diameter, resulting in an overall structure that resembles an inverted dome. The base of the cylinder is thermally anchored to a cryogenic cold head. Figure 1(a) illustrates a computer-aided design (CAD) model of the buffer gas cell and the affiliated volumes. Throughout this article, we define the symmetry axis of the cylinder as the y -axis, while the direction of propagation of the extracted molecular beam is the z -axis. Four short, straight cylindrical bores, all lying within the x - z plane, are connected to the main cell volume. A cross-sectional view of this plane is shown in Fig. 1(b), where bore ①, with a diameter of 4 mm , serves as the inlet for cold helium buffer gas. Bore ②, having a diameter of 6 mm and aligned along the z -axis, serves as the extraction channel and leads the molecules into the expansion volume. An aperture of diameter d is mounted at the entrance of this bore to define the exit orifice. In the

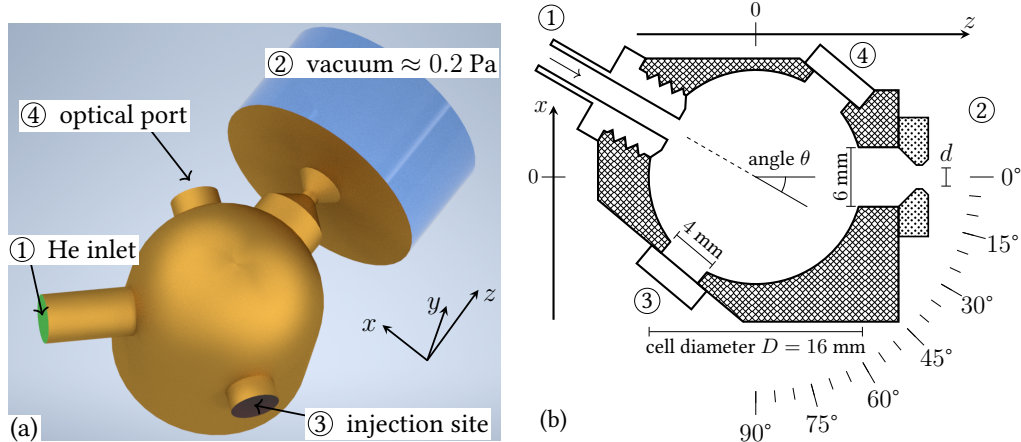


Figure 1. Geometry of the simulated buffer gas cell. (a) Three-dimensional rendering of the internal structure of the CBGB cell. The dome-shaped cell has four bores ①, ②, ③ and ④, and connects to three external volumes. The volume connected through ① represents the buffer gas inlet and is set to a constant pressure to simulate helium flow into the cell. The volume connected via ② corresponds to the low-pressure region into which the cold beam is extracted. Bore ③ represents the molecule injection port. In the simulation, a localized heat load is applied at this position to account for the accompanied heating effects. Opposite to ③, an optical viewport is mounted on bore ④. (b) Cross-sectional view of the buffer gas cell in the x - z -plane. The exit orifice diameter d and injection angle θ are varied to investigate their impact on the buffer gas flow dynamics and the molecular diffusion.

simulations, the angle θ between the buffer gas injection axis and the z -axis is varied in increments of 15° . Additionally, the diameter of the exit aperture d is varied across different simulation runs to permit a comparative analysis of flow dynamics under approximately same flow throughput but at different densities. Bore ③, also 4 mm in diameter, represents the injection port for the seed molecules. Located opposite to ③ is the bore ④ of equal diameter, included to represent a viewport for optical access. The injection angle of seed molecules is fixed at 130° relative to the z -axis.

3. Simulating and Benchmarking the Helium Flow

3.1. Basic settings

Helium is used as the buffer gas in our simulations. The helium flow is modeled over a range of throughputs from 12 to 87 standard cubic centimeters per minute (sccm), matching the regime of flow rates used in experiments [23]. This flow regime corresponds to Knudsen numbers $\text{Kn} < 0.1$, which permits the use of computational fluid dynamics (CFD) solvers, as also employed in previous work [18–20, 24].

We used COMSOL multiphysics with the microfluidics package in the slip flow regime to simulate the buffer gas flow. To do so, the full three-dimensional CAD design of the cell was imported into the simulation environment, where steady-state solutions to the Navier-Stokes equations were solved for helium, modeled as an ideal gas with mass $m_{\text{He}} = 4 \text{ amu}$, ratio of specific heat $\gamma = 5/3$, viscosity $\eta = 1.1078 \mu\text{Pa} \cdot \text{s}$ and heat conductivity $\kappa = 8.636 \text{ mW} \cdot \text{K}^{-1} \cdot \text{m}^{-1}$. The transport properties from Ref. [25] were taken considering a reservoir temperature $T_0 = 4.5 \text{ K}$.

Slip-flow boundary conditions were applied using a total tangential momentum accommodation coefficient $\alpha_t = 0.95$, which is chosen to be higher than the recommended value of 0.9 for technical surfaces at room temperature, and slightly lower than the 0.96 reported for helium interacting with oxygen-coated titanium surfaces [26]. The relatively high set value of $\alpha_t = 0.95$ was used to account for the effect that surface roughness causes the particles to scatter more diffusely from walls, bringing the coefficient closer to unity. However, we noted that a few test simulations performed with $\alpha_t = 0.90$ and 0.99 showed no qualitative impact on the flow behavior. The background pressure of the simulation volume was set to 0.2 Pa, as lower values resulted in numerical instabilities of the CFD solver. While this pressure is relatively high compared to high vacuum conditions typically present in the free-flight region of an experiment, it is not expected to significantly influence the flow pattern within the buffer gas cell.

3.2. Flow field and temperature

We begin by examining the overall behaviors of the CFD simulation through cross-validation of the resulting distributions of the vector velocity field \mathbf{u} , temperature T and flow speed represented by the Mach number \mathcal{M} . Each column in Fig. 2 displays the simulation output for \mathbf{u} , T , and \mathcal{M} (from top to bottom) for the parameter set indicated in the top row of the figure. In total, four different simulations are presented, all performed at a fixed buffer gas injection angle of $\theta = 0^\circ$, while other parameters including the orifice diameter d , external heat load Q , and flow throughput J were varied. In each plot, the components of the velocity field \mathbf{u} in the $y = 0$ plane, u_x and u_z , are sampled and displayed as black arrows. The orientation of each arrow indicates the direction of the local flow, while its length is scaled by $\tanh \sqrt{u_x^2 + u_z^2}$ to convey a stronger visual contrast of the flow patterns than a simple normalized field. The colored background shows the magnitude of $|\mathbf{u}|$ (upper panel), T (middle panel) and \mathcal{M} (lower panel) on the same $y = 0$ plane. Away from the $y = 0$ plane, the components u_x and u_z show similar distributions.

Focusing first on the flow fields depicted in panels (a) to (d), the buffer gas throughput J is gradually increased from 19 sccm to 86.9 sccm from left to right. As a result, the flow accelerates progressively, as shown by the increasingly darker shading and the lengthening of the arrows. In all plots, the flow within the cell exhibits a gradual acceleration toward the orifice while it remains subsonic. Supersonic expansion is observed at the exit orifice, as indicated by the darker shading in that region. This is accompanied by a noticeable temperature drop in the same region as illustrated in panels (e)–(h) on the middle row, and by increased Mach numbers in panels (i)–(l) on the bottom row.

The middle panels (e)–(h) display the temperature distributions. The cell walls are set at a constant temperature at $T_0 = 4.5$ K, which effectively acts as a thermal reservoir. The flow is expected to behave weakly compressible and quasi-isothermal, which agrees with the observations, where the temperature inside the cell remains nearly uniform at 4.5 K, and only changes notably in the vicinity of the exit orifice. The region with elevated temperature on the bottom right corresponds to the thermal load introduced by the injection of hot molecules. Heat loads

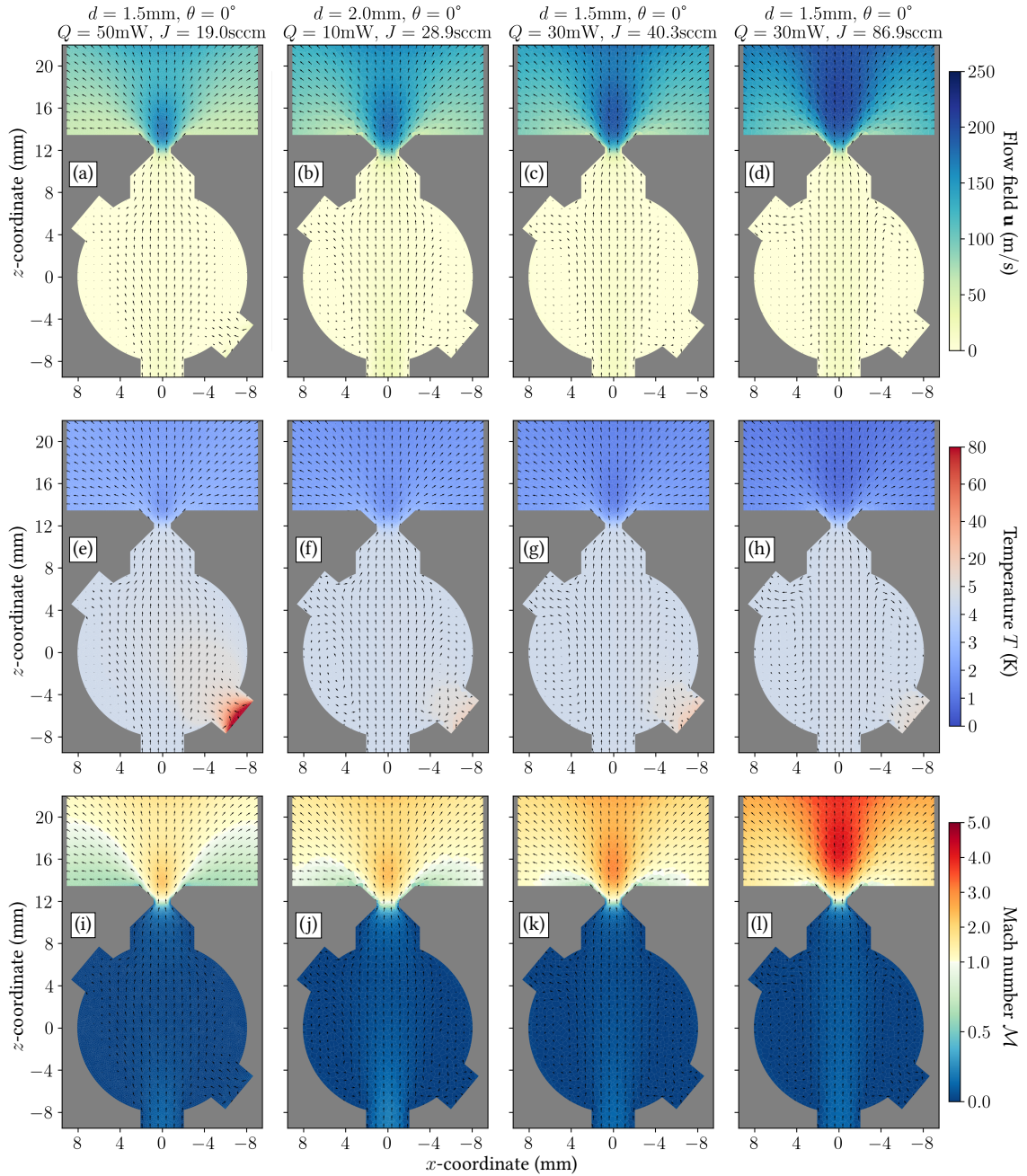


Figure 2. Top to bottom: (a)-(d) velocity field \mathbf{u} , (e)-(h) temperature T and (i)-(l) Mach number M distributions on the $y = 0$ plane simulated using four different parameter sets, as indicated by the legends on the top rows.

of $\{50, 10, 30, 30\}$ mW were applied to the simulations shown in panels (e)–(h), respectively. At the highest applied heat load of 50 mW, the temperature in the injection region reaches up to 80 K, which leads to disturbances in the local flow field. Nevertheless, the impact of this local heating on the flow towards the center of the cell remains negligible.

Panels (i)–(l) show the distribution of Mach numbers. The most prominent feature across all simulations is the onset of supersonic expansion at the orifice. As the buffer gas throughput increases from left to right, the maximal Mach number also increases. A cross examination of the corresponding temperature profiles in panels (e)–(h) reveal the characteristic cooling to temperatures between 2 K and

0.7 K associated with adiabatic expansion from the reservoir condition $T_0 \approx 4.5$ K.

The orifice diameter was also varied across the simulations. The two middle columns correspond to simulations with $d = 2.0$ mm, while the outer columns represent simulations with $d = 1.5$ mm. A comparison of the Mach number and temperature distributions between the first and second simulations, where similar Mach numbers are achieved, shows that a lower buffer gas throughput of 19.0 sccm is required for the smaller orifice diameter of 1.5 mm. This observation is consistent with expectations based on conventional supersonic expansion sources.

3.3. Effect of injection angle and vortex formation

Having benchmarked key outputs of the CFD simulation, we further investigate the influence of the buffer gas injection angle on the flow field. Panels (a)-(d) of Fig. 3 display a series of simulations with $d = 1.5$ mm, $Q = 30$ mW, $J = 26$ sccm, and $\theta = \{0^\circ, 15^\circ, 30^\circ, 45^\circ\}$. In all cases, the flow efficiently directs helium from the inlet to the orifice, with negligible velocity ($|\mathbf{u}| \approx 0$) near the cell walls and no evidence of backflow. The flow field in the vicinity of the orifice remains largely unaffected by variations in the injection angle. Similarly, no significant changes are observed in the expansion downstream of the orifice.

Panels (i)-(l) depict simulations performed with the same set of injection angles, but with increased buffer gas throughputs reaching $J = 69$ sccm. In contrast to flow patterns observed at lower throughputs, distinct vortical structures characterized by regions of backflow near the cell walls, where the axial velocity component satisfies $u_z < 0$, emerge in all configurations. The resulting recirculating flow re-directs the buffer gas inward, effectively refocusing it toward the central region of the cell. As the injection angle increases, the vortical structure becomes more asymmetric and shows a pronounced lobe on the lower right side of the cell, i.e., close to where seed molecules are injected into the cell. Despite these distortions within the cell, the flow pattern in the vicinity of the orifice and in the downstream expansion region remains largely unaffected by variations in the injection angle.

To gain insight into the vortex strength, we extract the vorticity of the flow, defined as $\mathbf{w} = \nabla \times \mathbf{u}$, which characterizes the local rotation of the field. In panels (e)-(h), the y -component of vorticity w_y is displayed, which shows strong features in the helium inlet line and changes sign across the center of the pipe. This is consistent with a shear profile in which the velocity magnitude varies transversely, as exemplified in the classical Hagen-Poiseuille flow. A similar sign reversal appears in the expansion region downstream of the orifice, where velocity gradients likewise lead to opposing vorticity components on either side of the central axis. Inside the cell, the vorticity distribution is mostly governed by the injected jet, which inherits characteristics of the helium flow in the pipe. At higher flow throughputs, as shown in panels (m)-(p), more complex structures emerge, which show as a separation between regions of positive and negative w_y on either side of the centerline, indicating the onset of vortical structures in which the circulation within the two hemispherical regions becomes more pronounced. Of particular interest is the influence of these vortical structures near the injection region of the molecules on the efficiency of molecular extraction, which we will explore in the next section.

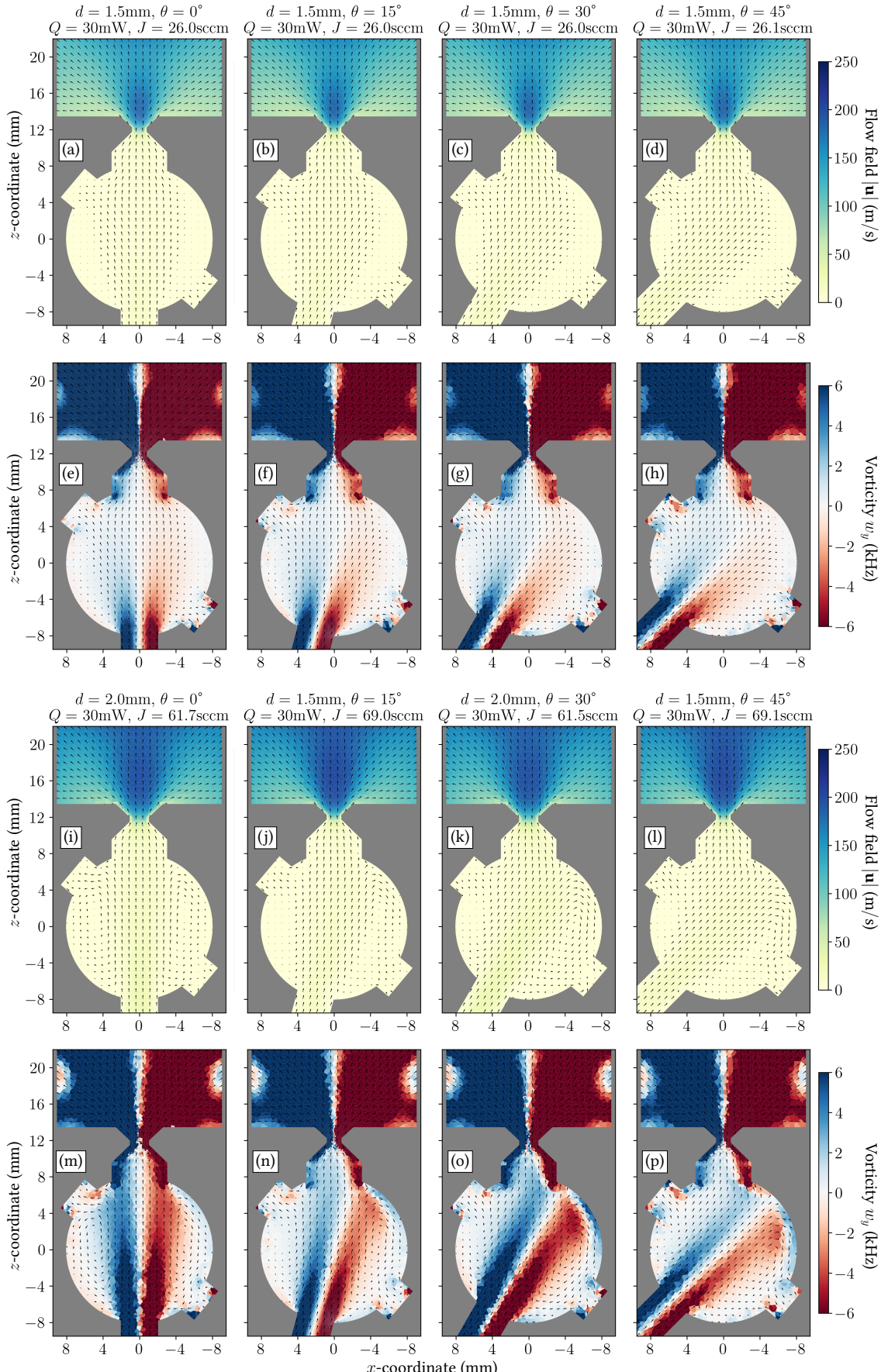


Figure 3. Simulated flow fields and vorticity distributions for buffer gas injection angles $\theta = \{0^\circ, 15^\circ, 30^\circ, 45^\circ\}$. (a)–(d) show the velocity field for a low-throughput of 26 sccm and (i)–(l) correspond to simulations with higher throughputs reaching 69 sccm. The respective out-of-plane component w_y of the vorticity field \mathbf{w} are displayed in (e)–(h) and (m)–(p).

4. Molecular Tracing through Direct-Simulation Monte Carlo

The CFD simulations provided an insight into the buffer gas flow characteristics. Due to the low partial pressure of the seed molecules, a fully hydrodynamic treatment of the combined gas mixture is not feasible. To capture the motion of molecules within the background helium flow, we implemented a particle-tracing algorithm in which the center-of-mass motion of molecules is tracked by solving Newton's equations, with stochastic terms incorporated to model elastic collisions with helium atoms. The helium velocity, density and temperature fields, obtained from the CFD simulations were treated as stationary inputs. This approach enables us to probe the thermalization and transport of molecules within the cell, and quantify the yield of molecule extraction at the orifice. The source code with example simulations is made available [22].

4.1. Basic settings

Specifically, the calculated flow $\mathbf{u}(\mathbf{r})$, number density $n(\mathbf{r})$ and temperature $T(\mathbf{r})$ from the CFD simulation were quantized to a grid of cubic voxels of side lengths $\delta = 500 \mu\text{m}$. Here, \mathbf{r} denotes the Cartesian coordinates of a given point inside the cell. We tested a few runs with finer meshes of $150 \mu\text{m}$ but found no systematic deviations besides the increased computational demands. The values of \mathbf{u} , n and T are stored in a look-up table to speed up the calculations. If several data points from the COMSOL mesh fall in the same voxel, their average values are taken. Voxels which did not coincide with mesh points were extrapolated by recursively taking the average of all non-empty nearest neighbors, resulting in a Voronoi-tesselation in Manhattan-metric with soft edges.

Our diffusion model is based on Ref. [20]. In short, the molecules are modeled as hard spheres of scattering cross section $\sigma = 1.2 \times 10^{-13} \text{ cm}^2$ with a mass $m = 128 \text{ amu}$, matching the properties of naphthalene as investigated in Ref. [23] and is expected to be sufficiently similar to medium-sized chiral or dye molecules, which could be explored further in subsequent cold beam experiments. The spheres move in straight paths at a velocity \mathbf{v} until an encounter with helium atoms is assigned to the particle. The average collision rate Γ is calculated according to

$$\Gamma = \sigma n(\mathbf{r}) \sqrt{|\mathbf{v} - \mathbf{u}(\mathbf{r})|^2 + \langle v \rangle_{\text{th}}^2}, \quad (1)$$

which accounts not only for the local thermal velocity of buffer $\langle v \rangle_{\text{th}}^2 = 8k_B T(\mathbf{r})/\pi m_{\text{He}}$ and instantaneous velocity of the molecule \mathbf{v} , but also the local flow velocity $\mathbf{u}(\mathbf{r})$ and number density of buffer gas $n(\mathbf{r})$.

In each simulation step, a molecule moves a distance $\Delta\mathbf{r} = \mathbf{v} \Delta t$ with the time step set to $\Delta t = 0.1/\Gamma$. After each time step, a collision was set to occur with a probability of 10%. In this way, the interval between two collisions for each individual molecule is allowed to vary drastically while the average is kept constant. As \mathbf{v} changes, so does Δt and the mean distance traveled between collisions. When the molecule moves at the same pace and direction as \mathbf{u} , it becomes stationary in the co-moving frame of the buffer gas flow and only the thermal motion of the buffer gas induces collisions. In this case, the mean free path $\lambda_m = v_m/\Gamma$

recovers the relation $\lambda = 1/(\sigma n \sqrt{1 + m/m_{\text{He}}})$, with the mean relative velocity amplitude $v_m = \sqrt{8k_B T/\pi m}$ [9, 27]. We compared two methods for assigning collision partners. First, the velocity of a collision partner was drawn randomly from a Maxwell-Boltzmann distribution. This approach may not account for the impact of the flow field as a moving frame of reference. In a second approach, we generated the three velocity components \mathbf{v}_{th} for 10 possible collision partners from a Gaussian distribution with variance $k_B T(\mathbf{r})/m$ for each assigned encounter and then drew randomly from this set with relative probabilities $\mathcal{P} \propto |\mathbf{v}_{\text{th}} + \mathbf{u} - \mathbf{v}|$, to account for the fact that faster particles are more likely to collide.

The back action of the diffusion of molecules on the buffer gas flow was neglected throughout.

4.2. Molecule trajectory and thermalization

The injected molecules were initialized at random positions on a circular disc of 4 mm diameter representing the injection needle, which was modeled with a heat load Q in the COMSOL simulations. The amplitude of the initial velocity vector was sampled from a Maxwell-Boltzmann distribution at 500 K, and the direction was chosen from a $\cos^2(\phi)$ distribution with ϕ the polar angle to the normal of the disc. The distribution of a single velocity component v_i with $i = \{x, y, z\}$ across all initialized molecules is therefore, non-thermal and biased in the direction away from the surface.

After each time step, the position of the molecule is checked. If a trajectory $\mathbf{r}(t)$ moves past the boundary of a voxel, the algorithm checks whether it has moved past the simulation volume. If this is not the case, the local values for n , T and \mathbf{u} are updated from the look-up table. If the molecule is found to be out of the simulation volume, the evaluation halts and the particle is considered lost to the wall unless it has reached the exit area.

The molecules were set to propagate for up to 10^9 collisions and a series of output data containing the time of propagation t , position \mathbf{r} and velocity \mathbf{v} was written to a file after every 10^3 collisions to keep the amount of data manageable. If a wall collision occurred within a threshold number of collisions K_{th} , a new particle was initialized to override the previous trajectory. The program was set to run until 10^5 trajectories with their number of collisions $K > K_{\text{th}}$ were saved.

To gain insight into the thermalization process, we generated normalized histograms $f(K, v_i) = N(K, v_i)/N(K)$ for each Cartesian velocity component v_i in all $N(K)$ molecules that have experienced K collisions. In Figs. 4(a)-(c), representative histograms for v_z , v_x , v_y of up to 1000 collisions are displayed. The color code from orange to purple and turquoise represents different values of K experienced. In v_z and v_x , a notable initial offset is present due to the $\cos^2(\phi)$ dependence of initial velocity. The maxima of the distributions gradually shift towards lower values and settle at zero with the increasing number of collisions. For v_y , the initial distribution $f(K=0, v_y)$ is centered at zero due to symmetry upon reflection on the x - z plane and approaches the familiar bell-curve while staying centered around zero. For all three components, no significant change in statistics was observed after the first 100 collisions.

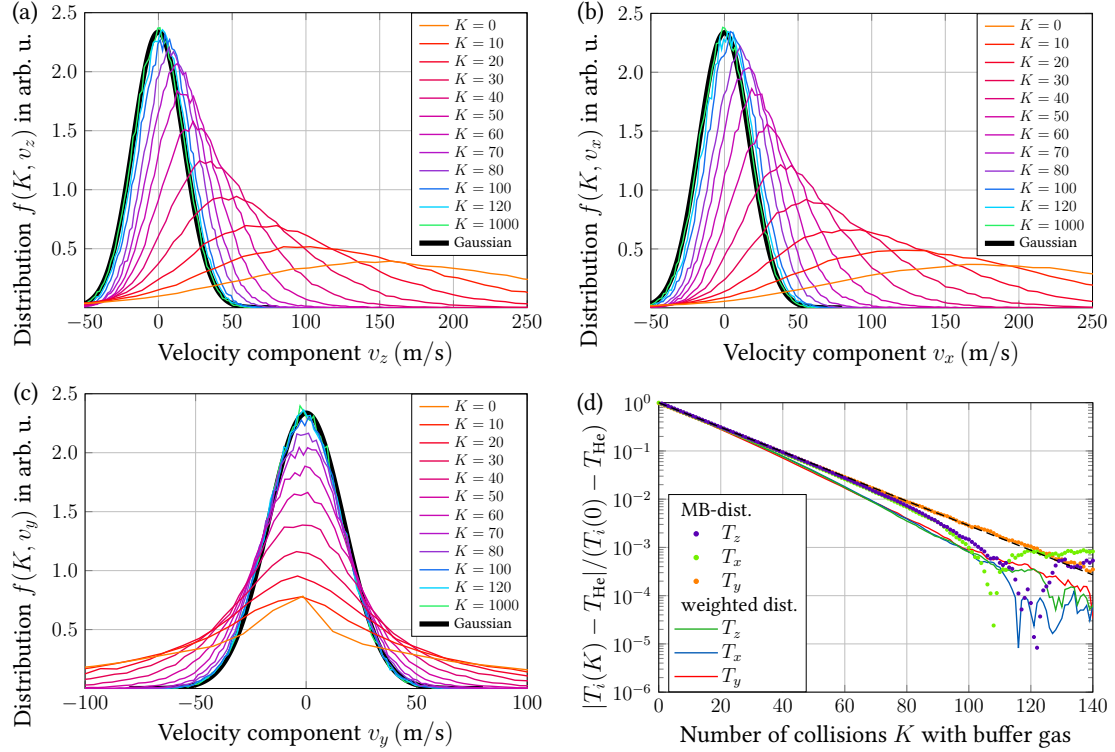


Figure 4. (a)-(c) The distribution f of velocity components v_i across all simulated molecules. This data was gathered from simulations with $d = 2.0 \text{ mm}$, $J = 58.8 \text{ sccm}$, helium injection angle of $\theta = 0^\circ$ and a cell diameter of 19 mm. Black lines in the background represent a Gaussian distribution with a temperature of 4.5 K. (d) The relative change of temperature $|T_i(K) - T_{\text{He}}| / (T_i(0) - T_{\text{He}})$ plotted as a function of number of collisions experienced.

By fitting a Gaussian function to each of the histograms, as illustrated by the black lines in Figs. 4(a)-(c), we assigned temperatures $T_i(K)$ to the three Cartesian degrees of freedom. For this, we saved the data from the first 200 collisions. The results are presented in Fig. 4(d), where the colored lines and dots show the data from the numerical simulations, and the dashed black line follows an analytic model

$$T_i(K) = T_{\text{He}} + (T_i(0) - T_{\text{He}}) \exp \left[\frac{-2Km m_{\text{He}}}{(m + m_{\text{He}})^2} \right] \quad (2)$$

provided in Ref. [9]. With both methods of sampling collision partners, we observe a drop in temperature $|T_i(K) - T_{\text{He}}|$ falling within one percent of the initial temperature difference in about 80 collisions. In addition to this global trend, we find that the data of T_y using direct sampling of a Maxwell-Boltzmann distribution recover the analytical formula the best. The reason could be that the buffer gas flow pattern is approximately symmetric upon reflection on the x - z plane, while for both two other axes, a mean relative velocity of the helium flow and initial velocity of the molecules is present.

A visible difference of the results using the two sampling methods appears after 40 collisions. The two-step sampling results in faster thermalization. The deviations could hence stem from the fact that the velocity of helium atoms participating in collisions was no longer normally distributed after being randomly sampled twice. With both methods, we observed that within 100 to 140 collisions, the temperature

difference between the molecules and the buffer gas reaches the level of 10^{-4} , hitting the numerical noise floor, which is expected considering our sample size of 10^5 .

4.3. Extraction efficiency

In the next step, we quantify the extraction efficiency of molecules in cells with different injection angles and operating at various flow throughputs. For each simulation, we evaluated $N_T \approx 10^5$ trajectories, whose final positions \mathbf{r}_f were extracted. We use a combination of azimuthal angle $\arctan(x/z)$ and the y -coordinate to uniquely represent \mathbf{r}_f , as the radial distance of almost all final positions equals the radius of the cell. The distributions of \mathbf{r}_f in four different simulations are shown in the upper row of Fig. 5. The molecules can be sorted into three groups. First, molecules that did not leave the source disc. They lie within the blue ellipse centered at $y = 0$ mm and $\arctan(x/z) = -130^\circ$ in the histogram. This number depended very strongly on the heating power Q and was sensitive to local fluctuations in \mathbf{u} . Second, the molecules that reached the exit orifice, corresponding to the ones landed in the area surrounded by the green ellipse. Their number is recorded as N_E . Third, molecules that left the starting region but did not terminate within the exit region are considered losses and contamination of the cell walls. Their number is recorded as N_L .

A first observation of the histograms reveals that a large number of molecules struck the wall within the injection disc shortly after their initialization. This is evident from the relatively strong intensity in the black circles in all plots. The density of molecules deposited on the inner wall is lower compared to that of the inlet and outlet area. Both low-throughput simulations in (a) and (c) feature a broad distribution of molecules between azimuthal angles from 10° to -135° and $y = -4$ mm to 6 mm, showing a relatively large amount of wall contamination. Both high-throughput simulations in (b) and (d) show more concentrated distribution in the input and exit areas, hinting at a higher extraction yield. To quantitatively compare different simulations, we define the extraction efficiency

$$\eta = \frac{N_E}{N_E + N_L} \quad (3)$$

of only the molecules which were successfully injected into the cell.

Out of surprise, the scenario shown in (d) of with $\theta = 45^\circ$ at $J = 69$ sccm gives the highest yield among the four simulations presented. To understand the differences in extraction behavior, we randomly sampled 25 trajectories of extracted molecules from each of the simulations and plotted their projection in the x - z plane, as displayed in Figs. 5(e)-(h). The change in color along each trajectory represents the time after initialization, as indicated by the color bar. The black arrows in the background indicate the helium flow field.

In the two low-throughput scenarios of (e) and (g), the molecules remained mostly in the half of the cell where they had been injected. Although individual trajectories are rather noisy due to the large number of collisions involved, they follow a general trend towards the exit in a mostly direct path. In stark contrast, the trajectories in the high-throughput regimes displayed in (f) and (h) seem to follow

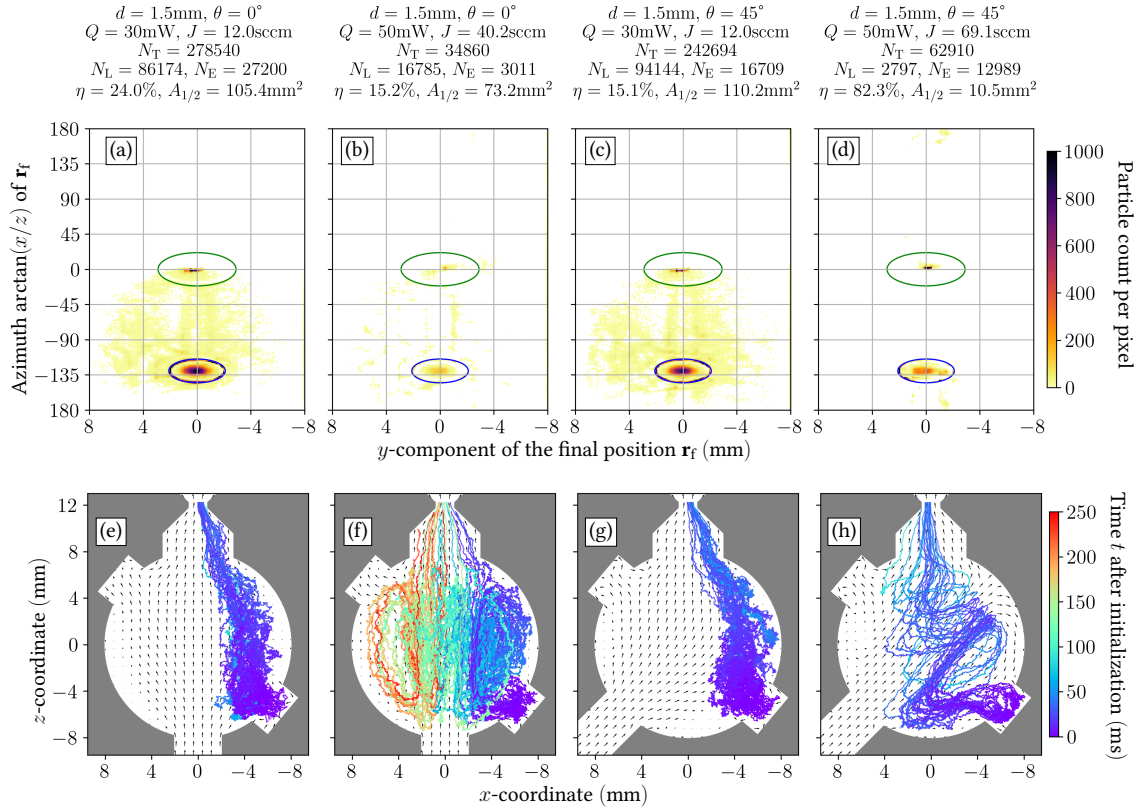


Figure 5. (a)-(d) Heat map histograms of last positions \mathbf{r}_f of molecules. Counts within the green ellipse at $y = 0$ mm, $\arctan x/z = 0$ have reached the exit and would participate in the expanding beam. Counts within the blue ellipse $y = 0$ mm, $\arctan x/z = -130^\circ$ got stuck near their initialization point. (e)-(h) 25 sample trajectories of molecules moving through the cell. Each curve changes color as a function of time. To keep the displayed data manageable, only positions after every 1000 collisions are shown.

nearly helical paths. While this may seem less efficient at first, the configuration $\theta = 45^\circ$ at $J = 69$ sccm outperforms all low-throughput simulations, where η reaches around 80%, which means eight of ten molecules that escaped the source disc arrive at the exit. In this scenario, shown in (h), the molecules are first drawn away from the source area by the strong vortex field toward the entrance of helium gas and then pushed straight through the center of the cell towards the orifice.

A summary of the extraction efficiencies obtained from a total of 115 simulations is presented in the left panel of Fig. 6 and detailed statistics on these simulations is listed in [Appendix A](#). In the low-throughput regime ($J < 30$ sccm), all geometries show low extraction efficiencies, mostly remaining below 25%. As J increases, configurations with inclined helium injection show a notable rise in extraction efficiency. In particular, three separate simulations with $\theta = 45^\circ$ at $J = 69$ sccm resulted in extraction yield all above 70%. Parallel to the extraction yield, we analyzed the equivalent coated median area $A_{1/2}$ of the pixels that make up $N_L/2$ of the molecules that landed on the inner surface of the cell. A smaller $A_{1/2}$ implies a reduced spread across the cell walls. The plot in the right panel of Fig. 6 confirms that the configuration of $\theta = 45^\circ$ in the high-throughput regime also shows minimal wall contamination.

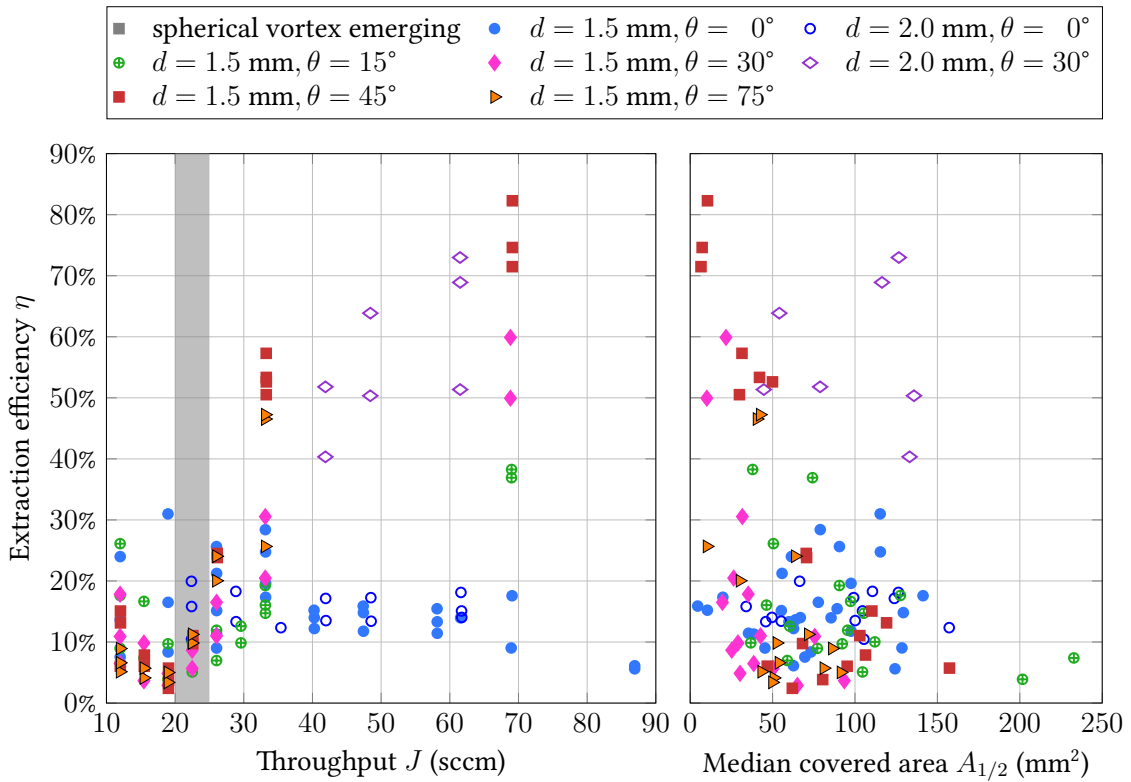


Figure 6. Extraction efficiency η plotted over throughput J and median covered area $A_{1/2}$. The gray vertical bar illustrate the flow range where vortices in the buffer gas flow emerge. For $\theta = 0^\circ$, efficiency goes down with J in an approximately linear fashion. For $\theta > 30^\circ$, a change in trend is observed after the onset of vortex formation around $J \approx 25 \text{ sccm}$ with the efficiency increasing and $A_{1/2}$ decreasing for higher throughput.

4.4. Extraction time

In the final step, we analyze the residence time τ in the cell for all successfully extracted molecules. Figure 7 presents the normalized histograms of residence time for simulations performed at four different injection angles, each evaluated at four different flow throughputs. In the low-throughput regime ($J = 12 \text{ sccm}$), different cell geometries result in similar extraction-time distributions, with the majority of molecules exiting the cell within 10 ms to 50 ms. As the flow rate increases, the geometry with $\theta = 0^\circ$ exhibits two additional peaks in the residence time distribution. The emergence of these peaks coincides with the flow regime of vortex formation in the buffer gas flow. A further observation of that the three maxima are close to evenly spaced could be the result of an integer number of revolutions in one of the vortex lobes before being extracted. This behavior is corroborated by the molecular trajectories shown in Fig. 5(f). The extraction time for the majority of molecules remains peaked at approximately 20 ms, with the peak position shifting slightly toward shorter times as the throughput increases, which is consistent with the corresponding rise in flow velocity.

For the scenarios of $\theta = 15^\circ$ and 30° , similar multi-peak distributions are observed. However, the maxima of the distributions switch to peaks at long time scales in the simulations with $J = 26 \text{ sccm}$ and 31 sccm . As the flow rate increases

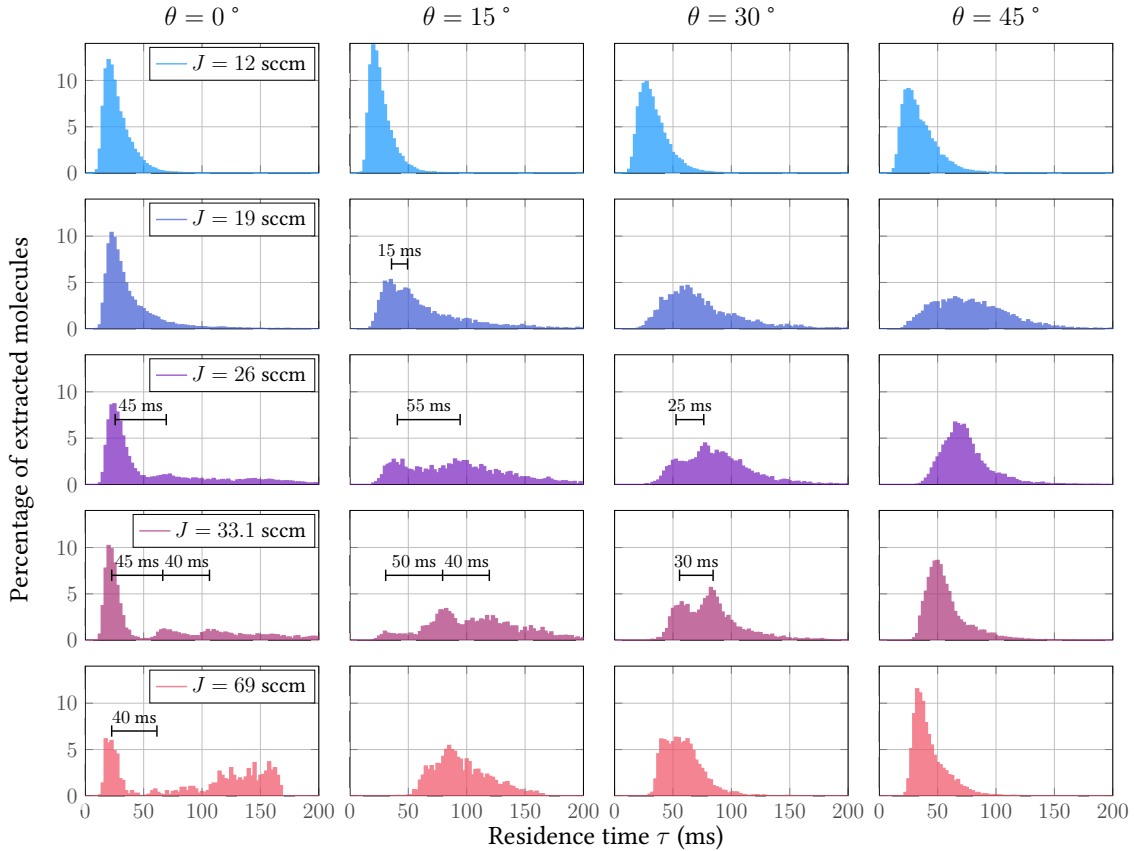


Figure 7. Histogram of residence times τ for different geometries θ with fixed $d = 1.5$ mm at different throughput J . With the emergence of the spherical vortex, several maxima appear beside the main peak which stays relatively consistent around $\tau \approx 25$ ms but changes in intensity. The new maxima appear regularly spaced, hinting at molecules traveling along the vortex for one or two additional full loops before exiting. At the steeper injection angle $\theta = 45^\circ$, this effect is reduced, possibly due to the wide side lobe of the vortex facing the injection side. The emergence of two or three beam intensity maxima after pulsed injection of molecules could be verified experimentally by time-of-flight measurements.

further, the peaks merge and a broad distribution takes over with the peak extraction time shifted to around 50 ms to 80 ms. This signifies that vortices in the buffer gas flow lead to delays in extraction and a larger uncertainty in the residence time.

For geometry with $\theta = 45^\circ$, no multi-peaked residence time distribution is observed. At throughputs above 19 sccm, increasing J results in a progressive narrowing of the distribution and a shift of the peak residence time toward approximately 30 ms, i.e., a focusing effect that both narrows down the distribution and allows fast extraction. This observation is in accordance with the increased extraction yield discussed in the previous section.

5. Conclusion

In summary, we have presented the numerical investigation of hydrodynamic effects in a cryogenic buffer gas beam source. A hybrid approach combining CFD simulations and particle tracing provided detailed insights into the buffer gas flow pattern, as well as the thermalization and extraction behaviors of the seed molecules.

The results show that key parameters such as the injection angle of the buffer gas and flow rate have subtle effects on the extraction efficiency. The geometry with a helium injection angle at 45° in the high-throughput regime shows unexpectedly advantageous features, including high extraction efficiency and narrow extraction time distributions. These results could be tested through velocity and time-of-flight measurements downstream of the cell in future experimental studies. While the flow rates considered in this work are at the upper limit of those reported in recent experimental setups [23, 28], the complete throughput regime should become accessible with increased pumping capacity. More generally, we hope that the numerical tools presented in this work [22] can assist future optimization work of buffer gas sources, including, for example, the design of more sophisticated sources involving multi-stages [16, 21] to reduce forward velocities and further lower the internal temperatures.

Acknowledgement

This work was funded by the Deutsche Forschungsgemeinschaft (DFG, German Research Foundation) — Project No. 328961117 — SFB 1319 ELCH (Extreme light for sensing and driving molecular chirality) and under Germany’s Excellence Strategy — Cluster of Excellence Matter and Light for Quantum Computing (ML4Q) EXC 2004/1 - 390534769.

References

- [1] Ríos JP. An Introduction to Cold and Ultracold Chemistry. 1st ed. Switzerland: Springer Nature; 2020.
- [2] Karman T, Tomza M, Pérez-Ríos J. Ultracold chemistry as a testbed for few-body physics. *Nat Phys.* 2024;20:722-9. Available from: <https://doi.org/10.1038/s41567-024-02467-3>.
- [3] Ziurys LM. Prebiotic Astrochemistry from Astronomical Observations and Laboratory Spectroscopy. *Annual Review of Physical Chemistry.* 2024;75(1):307-27. Available from: [https://www.annualreviews.org/content/journals/10.1146/annurev-physchem-090722-010849](https://www.annualreviews.org/content/journals/10.1146/annurevophyschem-090722-010849).
- [4] Cornish SL, Tarbutt MR, Hazzard KRA. Quantum computation and quantum simulation with ultracold molecules. *Nat Phys.* 2024;20:730-40. Available from: <https://doi.org/10.1038/s41567-024-02453-9>.
- [5] Deiß M, Willitsch S, Hecker Denschlag J. Cold trapped molecular ions and hybrid platforms for ions and neutral particles. *Nat Phys.* 2024;20:713-21. Available from: <https://doi.org/10.1038/s41567-024-02440-0>.
- [6] Langen T, Valtolina G, Wang D, Ye J. Quantum state manipulation and cooling of ultracold molecules. *Nat Phys.* 2024;20:702-12. Available from: <https://doi.org/10.1038/s41567-024-02423-1>.
- [7] DeMille D, Hutzler NR, Rey AM, Zelevinsky T. Quantum sensing and metrology for fundamental physics with molecules. *Nat Phys.* 2024;20:741-9. Available from: <https://doi.org/10.1038/s41567-024-02499-9>.
- [8] Campbell WC, Doyle JM. Cooling, Trap Loading, and Beam Production Using a Cryogenic Helium Buffer Gas. In: Krems R, Friedrich B, Stwalley WC, editors. *Cold Molecules.* 1st ed. Boca Raton: CRC Press; 2009. .

- [9] Hutzler NR, Lu H, Doyle JM. The Buffer Gas Beam: An Intense, Cold, and Slow Source for Atoms and Molecules. *Chem Rev.* 2012;112:4803–4827. Available from: <https://doi.org/10.1021/cr200362u>.
- [10] Vilas NB, Hallas C, Anderegg L, Robichaud P, Winnicki A, Mitra D, et al. Magneto-Optical Trapping and Sub-Doppler Cooling of a Polyatomic Molecule. *Nature.* 2022;606:70-4. Available from: <https://doi.org/10.1038/s41586-022-04620-5>.
- [11] Mitra D, Vilas NB, Hallas C, Anderegg L, Augenbraun BL, Baum L, et al. Direct laser cooling of a symmetric top molecule. *Science.* 2020;369(6509):1366-9. Available from: <https://www.science.org/doi/abs/10.1126/science.abc5357>.
- [12] Hofäss S, Padilla-Castillo JE, Wright SC, Kray S, Thomas R, Sartakov BG, et al. High-resolution isotope-shift spectroscopy of Cd i. *Phys Rev Res.* 2023 Jan;5:013043. Available from: <https://doi.org/10.1103/PhysRevResearch.5.013043>.
- [13] Röser D, Padilla-Castillo JE, Ohayon B, Thomas R, Truppe S, Meijer G, et al. Hyperfine structure and isotope shifts of the $(4s^2)^1S_0 \rightarrow (4s4p)^1P_1$ transition in atomic zinc. *Phys Rev A.* 2024 Jan;109:012806. Available from: <https://link.aps.org/doi/10.1103/PhysRevA.109.012806>.
- [14] Piskorski J, Patterson D, Eibenberger S, Doyle JM. Cooling, Spectroscopy and Non-Sticking of trans-Stilbene and Nile Red. *ChemPhysChem.* 2014;15(17):3800-4. Available from: <https://chemistry-europe.onlinelibrary.wiley.com/doi/abs/10.1002/cphc.201402502>.
- [15] Miyamoto Y, Tobaru R, Takahashi Y, Hiramoto A, Iwakuni K, Kuma S, et al. High-resolution spectroscopy of buffer-gas-cooled phthalocyanine. *Communications Chemistry.* 2022;5:161. Available from: <https://doi.org/10.1038/s42004-022-00783-4>.
- [16] White AD, Popa S, Mellado-Muñoz J, Fitch NJ, Sauer BE, Lim J, et al. Slow molecular beams from a cryogenic buffer gas source. *Phys Rev Res.* 2024 Dec;6:043232. Available from: <https://link.aps.org/doi/10.1103/PhysRevResearch.6.043232>.
- [17] Wright SC, Doppelbauer M, Hofäss S, Schewe HC, Sartakov B, Meijer G, et al. Cryogenic buffer gas beams of AlF, CaF, MgF, YbF, Al, Ca, Yb and NO – a comparison. *Molecular Physics.* 2023;121(17-18):e2146541. Available from: <https://doi.org/10.1080/00268976.2022.2146541>.
- [18] Singh V, Samanta AK, Roth N, Gusa D, Ossenbrüggen T, Rubinsky I, et al. Optimized cell geometry for buffer-gas-cooled molecular-beam sources. *Phys Rev A.* 2018;97(3):032704. Available from: <https://doi.org/10.1103/PhysRevA.97.032704>.
- [19] Gantner T, Koller M, Wu X, Rempe G, Zeppenfeld M. Buffer-Gas Cooling of Molecules in the Low-Density Regime: Comparison between Simulation and Experiment. *J Phys B: At Mol Opt Phys.* 2020;53. Available from: <https://doi.org/10.1088/1361-6455/ab8b42>.
- [20] Takahashi Y, Shlivko D, Woolls G, Hutzler NR. Simulation of Cryogenic Buffer Gas Beams. *Phys Rev Res.* 2021;3. Available from: <https://doi.org/10.1103/PhysRevResearch.3.023018>.
- [21] Singh V. Theoretical investigation of a two-stage buffer gas cooled beam source. *Cryogenics.* 2021;118:103335. Available from: <https://www.sciencedirect.com/science/article/pii/S001122752100093X>.
- [22] Cold Diffusion in Buffer-Gas Simulation;. <https://doi.org/10.5281/zenodo.16320104>.
- [23] Patterson D, Tsikata E, Doyle JM. Cooling and Collisions of Large Gas Phase Molecules. *Phys Chem Chem Phys.* 2010;12:9736-41. Available from: <https://doi.org/10.1039/C002764B>.
- [24] Skoff SM, Hendricks RJ, Sinclair CDJ, Hudson JJ, Segal DM, Sauer BE, et al. Diffusion, thermalization, and optical pumping of YbF molecules in a cold buffer-gas cell. *Phys Rev A.* 2011 Feb;83(2):023418. Available from: <https://link.aps.org/doi/10.1103/PhysRevA.83.023418>.
- [25] Hurly JJ, Mehl JB. ${}^4\text{He}$ Thermophysical Properties: New Ab Initio Calculations. *J Res Natl Inst Stand Technol.* 2007;112:75–94. Available from: <https://doi.org/10.6028/jres.112.006>.
- [26] Jousten K, Sharipov F. Grundlagen der exakten Berechnung stationärer Flüsse von verdünnten Gasen. In: Jousten K, editor. Handbuch Vakuumtechnik. 12th ed. Wiesbaden: Springer Vieweg; 2018. p. 195-232.
- [27] Bird GA. Molecular Gas Dynamics and the Direct Simulation of Gas Flows. 1st ed. Oxford:

- Clarendon Press; 1994.
- [28] Patterson D, Doyle JM. Bright, guided molecular beam with hydrodynamic enhancement. *The Journal of Chemical Physics*. 2007 04;126(15):154307. Available from: <https://doi.org/10.1063/1.2717178>.

Appendix A. Parameters and statistics of all particle trace simulations

Table A1: Input parameters and key output results for all the particle tracing simulations. Geometric parameters θ , d , and simulation parameters Q , J and mean buffer gas density in the cell $\langle n \rangle$ listed with corresponding particle tracing parameters N_T , N_L , N_E and calculated mean extraction time $\langle \tau \rangle$, median covered area $A_{1/2}$ and extraction efficiency η . All the 115 simulations are available on Zenodo [22].

θ	d	Q	J	$\langle n \rangle$	N_T	N_L	N_E	$\langle \tau \rangle$	$A_{1/2}$	η
	(mm)	(mW)	(sccm)	(cm $^{-3}$)				(ms)	(mm 2)	%
0°	1.5	5	12.00	$6.25 \cdot 10^{16}$	1390256	97706	7963	78	70	7.5
0°	1.5	10	12.01	$6.22 \cdot 10^{16}$	446589	107955	17029	135	64	13.6
0°	1.5	30	12.00	$5.99 \cdot 10^{16}$	278540	86174	27200	123	61	24
0°	1.5	10	18.97	$9.45 \cdot 10^{16}$	503491	62484	5705	112	73	8.4
0°	1.5	30	18.97	$9.26 \cdot 10^{16}$	186096	82149	16237	82	78	16.5
0°	1.5	50	18.96	$8.96 \cdot 10^{16}$	212883	72466	32534	72	115	31
0°	1.5	5	26.05	$1.27 \cdot 10^{17}$	674900	8136	1036	150	39	11.3
0°	1.5	10	26.03	$1.27 \cdot 10^{17}$	410594	24186	2395	135	45	9.0
0°	1.5	10	26.05	$1.27 \cdot 10^{17}$	423709	23367	4171	127	55	15.1
0°	1.5	30	26.05	$1.25 \cdot 10^{17}$	97651	41224	11115	98	56	21
0°	1.5	50	26.02	$1.23 \cdot 10^{17}$	100507	43196	14890	85	91	26
0°	1.5	5	33.18	$1.59 \cdot 10^{17}$	519723	3472	728	138	20	17.3
0°	1.5	10	33.18	$1.59 \cdot 10^{17}$	453490	10256	2501	134	98	19.6
0°	1.5	30	33.17	$1.58 \cdot 10^{17}$	92320	27264	8970	133	115	25
0°	1.5	50	33.14	$1.56 \cdot 10^{17}$	67058	27680	10983	120	79	28
0°	1.5	10	40.27	$1.91 \cdot 10^{17}$	276370	4963	690	113	63	12.2
0°	1.5	30	40.26	$1.90 \cdot 10^{17}$	57742	15449	2514	97	67	14.0
0°	1.5	50	40.23	$1.88 \cdot 10^{17}$	34860	16785	3011	135	10.4	15.2
0°	1.5	10	47.42	$2.23 \cdot 10^{17}$	252658	2451	327	95	98	11.8
0°	1.5	30	47.42	$2.22 \cdot 10^{17}$	63019	11541	2007	111	129	14.8
0°	1.5	50	47.39	$2.21 \cdot 10^{17}$	30832	13170	2487	111	4.6	15.9
0°	1.5	10	58.17	$2.71 \cdot 10^{17}$	205100	1038	134	110	35	11.4
0°	1.5	30	58.16	$2.70 \cdot 10^{17}$	83936	8129	1249	45	60	13.3
0°	1.5	50	58.14	$2.69 \cdot 10^{17}$	30503	9861	1802	41	89	15.5
0°	1.5	10	68.94	$3.18 \cdot 10^{17}$	170229	514	51	28	128	9.0
0°	1.5	30	61.57	$3.19 \cdot 10^{17}$	136222	6712	1089	55	85	14.0
0°	1.5	50	69.07	$3.18 \cdot 10^{17}$	40831	9682	2065	38	141	17.6
0°	1.5	10	86.92	$3.98 \cdot 10^{17}$	125713	215	14	89	63	6.1
0°	1.5	30	86.92	$3.98 \cdot 10^{17}$	123289	2104	125	64	124	5.6
0°	2.0	10	22.40	$6.10 \cdot 10^{16}$	301096	79187	14878	45	34	15.8
0°	2.0	30	22.37	$5.88 \cdot 10^{16}$	248630	82246	20493	39	66	19.9
0°	2.0	5	22.39	$6.12 \cdot 10^{16}$	641844	54046	6309	29	105	10.5
0°	2.0	10	28.87	$7.70 \cdot 10^{16}$	240742	48489	7460	52	46	13.3
0°	2.0	30	28.84	$7.52 \cdot 10^{16}$	128037	51533	11540	38	111	18.3
0°	2.0	10	35.40	$9.29 \cdot 10^{16}$	186236	28962	4080	33	157	12.3
0°	2.0	10	41.96	$1.09 \cdot 10^{17}$	205171	20255	3164	33	100	13.5
0°	2.0	30	41.92	$1.07 \cdot 10^{17}$	60302	27078	5602	28	124	17.1

0°	2.0	10	48.54	$1.24 \cdot 10^{17}$	203310	13918	2155	36	55	13.4
0°	2.0	30	48.50	$1.23 \cdot 10^{17}$	48897	21322	4450	70	99	17.3
0°	2.0	10	61.74	$1.56 \cdot 10^{17}$	196596	6440	1051	73	50	14.0
0°	2.0	30	61.71	$1.55 \cdot 10^{17}$	34084	13742	2442	81	105	15.1
0°	2.0	50	61.62	$1.53 \cdot 10^{17}$	29636	14569	3225	65	126	18.1
15°	1.5	5	11.98	$6.25 \cdot 10^{16}$	849538	59968	5903	103	77	9.0
15°	1.5	10	11.99	$6.22 \cdot 10^{16}$	378291	93373	19973	88	128	17.6
15°	1.5	30	11.99	$6.00 \cdot 10^{16}$	210648	78020	27574	129	50	26
15°	1.5	10	15.46	$7.84 \cdot 10^{16}$	307772	65179	5199	96	233	7.4
15°	1.5	30	15.46	$7.64 \cdot 10^{16}$	151923	70967	14186	141	97	16.7
15°	1.5	10	18.96	$9.45 \cdot 10^{16}$	292436	38122	1542	111	202	3.9
15°	1.5	30	18.97	$9.28 \cdot 10^{16}$	84827	45558	4896	130	92	9.7
15°	1.5	10	22.49	$1.11 \cdot 10^{17}$	282795	21116	1133	110	105	5.1
15°	1.5	30	22.49	$1.09 \cdot 10^{17}$	51531	27794	3095	97	112	10.0
15°	1.5	10	26.03	$1.27 \cdot 10^{17}$	265554	12152	910	97	59	7.0
15°	1.5	30	26.03	$1.25 \cdot 10^{17}$	39484	20677	2802	93	96	11.9
15°	1.5	10	29.59	$1.43 \cdot 10^{17}$	269103	7315	800	48	37	9.9
15°	1.5	30	29.59	$1.42 \cdot 10^{17}$	35444	17249	2486	44	60	12.6
15°	1.5	10	33.15	$1.59 \cdot 10^{17}$	430029	6985	1205	35	105	14.7
15°	1.5	30	33.15	$1.58 \cdot 10^{17}$	59091	22924	4381	62	46	16.0
15°	1.5	50	33.13	$1.56 \cdot 10^{17}$	44586	22699	5412	46	91	19.3
15°	1.5	30	69.00	$3.19 \cdot 10^{17}$	136221	4213	2611	88	38	38
15°	1.5	50	68.99	$3.18 \cdot 10^{17}$	39740	7693	4501	75	74	37
30°	1.5	5	11.98	$6.25 \cdot 10^{16}$	837304	76668	5301	98	39	6.5
30°	1.5	10	11.99	$6.23 \cdot 10^{16}$	407908	110141	13485	89	76	10.9
30°	1.5	30	11.99	$6.03 \cdot 10^{16}$	282836	94635	20538	98	35	17.8
30°	1.5	10	15.45	$7.85 \cdot 10^{16}$	380417	81867	3103	88	94	3.7
30°	1.5	30	15.46	$7.68 \cdot 10^{16}$	196777	87819	9579	93	29	9.8
30°	1.5	10	18.96	$9.46 \cdot 10^{16}$	295186	48391	1440	83	65	2.9
30°	1.5	30	18.96	$9.32 \cdot 10^{16}$	120554	61590	3146	49	30	4.8
30°	1.5	10	22.49	$1.11 \cdot 10^{17}$	253987	29212	1757	42	50	5.7
30°	1.5	30	22.49	$1.10 \cdot 10^{17}$	71110	35967	3408	47	25	8.7
30°	1.5	10	26.03	$1.27 \cdot 10^{17}$	229750	18337	2268	39	43	11.0
30°	1.5	30	26.03	$1.26 \cdot 10^{17}$	51833	23680	4678	43	20	16.5
30°	1.5	10	33.13	$1.59 \cdot 10^{17}$	254923	7786	2004	36	26	20
30°	1.5	30	33.13	$1.58 \cdot 10^{17}$	42481	14978	6588	32	32	31
30°	1.5	30	68.83	$3.19 \cdot 10^{17}$	99461	4251	4241	60	10.1	50
30°	1.5	50	68.83	$3.18 \cdot 10^{17}$	40071	5603	8369	56	22	60
30°	2.0	10	41.88	$1.09 \cdot 10^{17}$	539833	40169	27154	57	133	40
30°	2.0	30	41.89	$1.08 \cdot 10^{17}$	173132	48571	52188	44	79	52
30°	2.0	10	48.42	$1.25 \cdot 10^{17}$	511826	23439	23761	38	136	50
30°	2.0	30	48.43	$1.24 \cdot 10^{17}$	148931	31506	55685	85	54	64
30°	2.0	10	61.50	$1.56 \cdot 10^{17}$	475344	11488	12128	86	45	51
30°	2.0	30	61.51	$1.56 \cdot 10^{17}$	158521	23399	51857	75	116	69
30°	2.0	50	61.49	$1.54 \cdot 10^{17}$	133082	23047	62265	67	127	73
45°	1.5	0	12.02	$6.28 \cdot 10^{16}$	1572851	10250	659	53	47	6.0
45°	1.5	10	12.04	$6.25 \cdot 10^{16}$	340580	95893	14505	42	119	13.1
45°	1.5	30	12.04	$6.04 \cdot 10^{16}$	242694	94144	16709	36	110	15.1
45°	1.5	10	15.52	$7.86 \cdot 10^{16}$	423284	75130	4819	59	95	6.0
45°	1.5	30	15.52	$7.68 \cdot 10^{16}$	204584	100972	8619	46	106	7.9
45°	1.5	0	19.02	$9.49 \cdot 10^{16}$	878386	5088	126	93	62	2.4
45°	1.5	10	19.03	$9.48 \cdot 10^{16}$	425021	53683	2145	87	80	3.8
45°	1.5	30	19.04	$9.33 \cdot 10^{16}$	119523	66396	4031	79	157	5.7
45°	1.5	10	22.57	$1.11 \cdot 10^{17}$	342664	32101	3464	92	68	9.7
45°	1.5	30	22.58	$1.10 \cdot 10^{17}$	80006	41132	5109	88	103	11.1
45°	1.5	10	26.13	$1.27 \cdot 10^{17}$	268700	18011	5847	87	70	25

45°	1.5	30	26.14	$1.26 \cdot 10^{17}$	68295	28653	8964	75	71	24
45°	1.5	0	33.26	$1.59 \cdot 10^{17}$	373408	2015	2703	71	31	58
45°	1.5	10	33.27	$1.59 \cdot 10^{17}$	198845	7061	7208	65	30	51
45°	1.5	30	33.29	$1.58 \cdot 10^{17}$	61025	12043	13371	59	50	53
45°	1.5	50	33.27	$1.57 \cdot 10^{17}$	61977	18379	21015	56	42	53
45°	1.5	10	69.10	$3.19 \cdot 10^{17}$	111352	1383	3467	48	6.6	72
45°	1.5	30	69.11	$3.19 \cdot 10^{17}$	85448	2918	8582	45	7.3	75
45°	1.5	50	69.11	$3.18 \cdot 10^{17}$	62910	2797	12989	39	10.5	82
75°	1.5	5	11.97	$6.25 \cdot 10^{16}$	1081599	74844	4050	53	43	5.1
75°	1.5	10	11.98	$6.23 \cdot 10^{16}$	492645	111115	7851	50	54	6.6
75°	1.5	30	11.98	$6.07 \cdot 10^{16}$	304997	103127	10115	43	86	8.9
75°	1.5	10	15.44	$7.85 \cdot 10^{16}$	497902	86481	3716	60	51	4.1
75°	1.5	30	15.44	$7.72 \cdot 10^{16}$	255930	103781	6287	53	81	5.7
75°	1.5	10	18.93	$9.46 \cdot 10^{16}$	461112	56518	1982	80	50	3.4
75°	1.5	30	18.94	$9.36 \cdot 10^{16}$	168940	76173	4026	73	91	5.0
75°	1.5	10	22.46	$1.11 \cdot 10^{17}$	422752	34474	3763	87	53	9.8
75°	1.5	30	22.46	$1.10 \cdot 10^{17}$	126971	54663	6935	79	72	11.3
75°	1.5	10	26.00	$1.27 \cdot 10^{17}$	403659	21127	5293	76	30	20
75°	1.5	30	26.01	$1.26 \cdot 10^{17}$	101761	36738	11634	71	64	24
75°	1.5	10	33.10	$1.59 \cdot 10^{17}$	501497	14368	4959	62	10.2	26
75°	1.5	30	33.11	$1.59 \cdot 10^{17}$	111518	24493	21310	58	41	47
75°	1.5	50	33.11	$1.58 \cdot 10^{17}$	84322	24828	22230	56	42	47